Materials & Design 265 (2026) 115937

Contents lists available at ScienceDirect

Materials & Design

journal homepage: www.elsevier.com/locate/matdes

Efficient method for numerically generating High-Density wood fiber network microstructure models

Bin Chen [a,*], Erfan Oliaei [a], Lars A. Berglund [a,b]

[a] Wallenberg Wood Science Center, Department of Fiber and Polymer Technology, KTH Royal Institute of Technology, SE-10044 Stockholm, Sweden
[b] Laboratory of organic electronics, Linköping University, 60221 Norrköping, Sweden

ARTICLE INFO

Keywords:
Wood fiber network
Representative volume element
3D microstructure
Optical scattering
Molded fibers
High density

ABSTRACT

Realistic 3D microstructure models of wood fiber networks (WFNs, e.g., paper, molded fibers, hot-pressed fibers, etc.) are of interest for numerical modeling of mechanical, optical, and other physical properties. One challenge is to numerically describe 3D high-density WFN (HD-WFN) models with complex fiber shapes without fiber overlapping. An efficient method is proposed to generate 3D HD-WFN microstructures with porosities as low as 21.5% while without fiber overlapping. The HD-WFN microstructures are obtained by compressing an initially sparse structure using a geometrically designed 3D displacement field. The sparse structure can be optimized to obtain a very low-porosity HD-WFN by reducing the local fiber clustering. The method can generate HD-WFNs with designated shapes (e.g., molded shapes) and varied structural parameters, including fiber width, orientation, location, and material thickness. Each interfiber bond and local material axis in the HD-WFN models can be determined for numerical simulation of properties. The optical scattering of transparent HD-WFN models (polymer matrix composites, transparent paper) is numerically studied using ray tracing methods. The open-source code is available on GitHub, and it can be used to obtain a large dataset for deep learning modeling.

1. Introduction

Wood fiber networks (WFNs) can be used to replace fossil-based plastics [1–3] in packaging applications, including packaging for industrial products and food trays [4]. WFNs, including paper, molded fibers [5], and hot-pressed fiber networks [6] are porous materials. They can be considered as composites of fibers and air, where a higher fiber volume fraction V_f or lower porosity (P = 1-V_f) improves the mechanical properties of WFN significantly. For instance, a conventional kraft paper with relatively high porosity (P of 55–65%) has an elastic modulus of ~ 2 GPa and a strength of 12–30 MPa [7]. Hot-pressed high-density unbleached kraft WFN (P of ~ 25%) can reach a modulus of 10–13 GPa and a strength of 100–155 MPa [6,8]. Material design and application of those high-density wood fiber networks (HD-WFNs) should be supported by thorough investigations of structure–property relationships. Experimental approaches have limitations [9].

Materials design, development, and structure–property understanding would be aided by numerical modeling, such as the computational homogenization-based representative volume element (RVE) model. The RVE is the smallest volume that can represent the macroscopic material properties [10]. For WFN, a realistic microstructure is the starting challenge [11]. Simon [12] classified WFN paper microstructure models into four major categories: fiber networks reconstructed from micro-CT images, structured networks, synthetic networks with random distributions, and synthetic networks with statistical distributions. Inspired by the review from Bargmann et al. [13], we classify the RVE generation method for WFNs into two categories: micro-CT-based methods and geometrical methods.

The RVEs generated from micro-CT images are close to the real WFN microstructures. The volume images of fiber-reinforced biodegradable polymer composites recorded by micro-CT can directly function as the RVE [14] for numerical simulation after image processing. The statistical parameters of the fiber and fiber network geometries can be obtained from the analysis of micro-CT images using image processing techniques [15]. The generation of each RVE requires a real micro-CT image. For deep learning approaches, this is a limitation since large datasets are required. Another limitation is that parametric studies are difficult to perform since systematic variations in fiber geometries and orientation distributions in the microstructure model cannot be provided straightforwardly.

Geometrical methods for 3D WFN microstructure model generation tend to be simpler. The microscopic fiber network structure is generated

* Corresponding author.
E-mail address: binchen@kth.se (B. Chen).

https://doi.org/10.1016/j.matdes.2026.115937
Received 4 November 2025; Received in revised form 16 February 2026; Accepted 27 March 2026
Available online 27 March 2026

"synthetically" based on simplifying assumptions. To create 3D high-density WFN (HD-WFN) microstructures, challenges include 1) reaching high relative density (V_f) or low porosity (P), 2) reaching a microstructural description that can accurately simulate the real network structure, and 3) avoiding fiber overlap (parts of two fibers occupying the same space). Liu et al. [16] proposed a 2D lattice model to simulate the failure of paper due to sequential fiber or inter-fiber bond fracture. 3D fiber networks are more realistic but at a higher computational cost. Ma et al. [17] constructed a 3D periodic random beam network based on a geometrical method. They simulated the cross-linkers into the fiber network by inserting beam elements between the intersected fibers. This method is more suitable for low-density materials (low V_f). The fibers are straight beams, which are different from the real WFN material.

Niskanen and Alava proposed a deposition technique, which is an effective geometrical method [18]. The fibers are sequentially deposited [19]. The deposited fibers can bend and conform geometrically to the fibers below. Such 3D fiber network microstructures have been used to simulate deformation and failure behavior [19]. The advantage of this method is the controlled distribution of fiber geometry, including length, cross-sectional shape, and orientation. One limitation is that low porosity (or high V_f) is challenging. Verho et al. [20] generated the WFNs by combining micro-CT images and synthetic networks with statistical distributions. They first analyzed the micro-CT images for morphological statistics. The RVE is then constructed based on size, orientation and shape statistics from the analysis. The construction step to generate a single RVE is laborious and the final V_f value was 25.5% (P = 74.5%). It is difficult to reach high V_f in the RVEs generated by this method.

The porosity of hot-pressed WFNs can be as low as 25% [6] and possibly even less. Compressing a sparse microstructure is an effective way to improve V_f. Sliseris et al [21] proposed to first obtain statistical parameters from micro-CT images. An initial high-porosity (P = 78%) fiber network is generated by using a fiber lay-down process via the commercial software GeoDict [22]. The volume is compressed using an efficient Fast Fourier Transform (FFT) based method to obtain a higher density. The reported V_f of the compressed fiber network is 40 % (porosity P = 60 %). A similar method has been used to model the 3D microstructure of compressed gas-diffusion layers [23]. Here, the fiber network is compressed with a simple displacement field, which may lead to fiber overlapping. Their algorithm, therefore, requires an additional iterative avoidance algorithm to fix the fiber overlapping issue.

The commercial product, like GeoDict (Math2Market GmbH, Germany) [22] has been widely used to generate the paper structures [21,24,25] by using the sequential deposition and local relaxation strategy. The generated models have been used to study airflow and particle transport via simulation [24] and to investigate the structure–mechanical property relationships using deep learning [25]. With this tool, it is challenging to achieve a very high V_f without fiber overlapping or significant algorithm convergence issues. The ProcessGeo modules in GeoDict can compress a high-porosity structure based only on the geometry information to reach a low porosity. However, the original structural morphology will limit the porosity that the material can reach due to the possible local fiber clustering. Additionally, the compression usually leads to very wavy fibers, which is not always realistic in WFNs. Accurate tracking of the fiber orientation tensor at every voxel is also challenging, which is important for material property assignment.

To our knowledge, no prior method achieves numerical models of realistic WFNs with P down to around 20% without fiber overlapping. Here, we develop a simple and efficient method for this purpose. The WFNs can reach very low P without fiber intersection. A sparse microstructure is geometrically compressed using a carefully designed 3D displacement field. Initially, a group of fibers is generated, and they are assumed to have an elliptical cross-section to facilitate mathematical description. A collapsed cross-sectional shape is typical for chemically processed wood pulp fibers [26], and here the elliptical shape represents any wood pulp fiber hot-pressed to high V_f. These fibers are stacked one by one to form a thick, low-density (or high-porosity) structure. A 3D compressive displacement field is retrieved from the initial sparse structure by assuming that 1) the fibers are incompressible and 2) the "interfiber" air is uniformly compressed. The 3D displacement field is obtained directly from volume image analysis rather than stress analysis for efficiency. To reduce porosity, the sparse WFN is compressed using the retrieved compressive displacement field. This method means that fiber overlapping is naturally avoided; parts of neighboring fibers cannot occupy the same space.

The former strategy still struggles to reach very low porosity due to the possible local fiber clustering. Therefore, an optimization strategy is suggested. The idea is to reduce the local fiber clustering in the initial sparse microstructure by optimizing the location of each fiber using the particle swarm algorithm. The optimization step can further reduce the porosity to around 20% without fiber overlapping or obvious weight loss. The obtained porosity is very close to the lowest porosity (25% [6] or even lower) of WFNs reported in literature. The generated microstructure models match well with the real 3D HD-WFN (porosity around 20%) microstructural images obtained by scanning electron microscope (SEM).

The proposed method can also numerically simulate WFNs with complicated geometry (such as double curvature or folded shapes), enabling a geometrical model of the molded fibers. The method also allows for segmenting every single fiber in the compressed WFNs, locating fiber bond distributions (fiber surfaces close to each other), and obtaining local principal material axes distributions of distorted fibers, which are critical for fiber waviness analysis and physical properties modeling. To facilitate the use of this method, the source code for 3D HD-WFN microstructure model generation is released on GitHub.[1]

The generated HD-WFN models are then used to study the optical scattering of transparent wood fiber composites and paper using ray tracing [27]. The optical scattering is assumed to result from the refractive index (RI) difference between the fibers and the matrix (air or polymer). The ray tracing method tracks the paths of a group of rays through the 3D microstructures using geometrical optics, and optical haze can be obtained (scattering at large angles, >2.5°). The ray tracing is very efficient since the time-consuming 3D microstructure meshing is avoided. In this work, the effect of fiber orientation distribution on the optical scattering of WFN is first evaluated. Additionally, the optical scattering behavior of the WFN and WFN-polymer composites is also compared.

2. Method

2.1. Real HD-WFN materials and processing

We used never-dried, high-lignin, unbleached softwood kraft pulp supplied by SCA Munksund AB. These fibers, showing minimal mechanical damage, are straight and have favorable eco-indicators [6]. Average fiber length is ~ 2.0 mm, width 34.7 µm, with a low kink index, as reported in [28]. Chemical composition is ~ 13.7% lignin, 67% cellulose, 9.7% glucomannan, and 9.5% xylan [6,28].

Aqueous fiber suspensions (0.3–0.4 wt%) were vacuum-filtered into wet sheets using a Finnish hand-sheet former (Lorentzen & Wettre, Sweden). Sheets were cold-pressed, then hot-pressed at 185 °C for 20 min to form dense fiber networks with random in-plane orientation [6]. Oriented sheets were prepared using a dynamic sheet former (Formette Dynamic, Fibertech AB, Sweden) at 1200 rpm with 0.2 wt% pulp suspension. Both sheet types had a basis weight of ~ 200 g/m^2 and were pressed identically. Final sheet thickness was ~ 170–180 µm. Estimated porosity was ~ 24% for random sheets and ~ 20% for oriented sheets,

[1] https://github.com/BinChenOPEN/3D-High-Density-Wood-Fiber-Network-Model.

calculated from dimensions, weight, and an assumed lignocellulose (skeleton) density of 1.5 g/cm^3.

2.2. Real microstructural analysis using a scanning electron microscope

Surface and cross-section microstructures were studied using a SEM (TM-1000, Hitachi) and FE-SEM (S-4800, Hitachi). Cross-sections of hot-pressed WFN sheets were embedded in epoxy and polished. Samples were sputter-coated with Pt-Pd for 20–60 s using a Cressington 208HR coater.

2.3. HD-WFN microstructure model simulation

2.3.1. Method summary

The flowchart for 3D HD-WFN model generation is summarized in Fig. 1. A group of elliptical fibers is generated analytically. These fibers are stacked one by one to form a sparse WFN (Fig. 1(a)). The location of each fiber is optimized (Fig. 1(b)) under a constraint of lower porosity, which is an important step to reach a very low porosity (high density). The center part is then clipped (Fig. 1(b)) to avoid the inhomogeneity in the boundary. A 3D compressive displacement map (Fig. 1(c)) is then generated from the sparse WFN based on only geometrical information, which is the key step in this method. The sparse WFN is compressed by using this 3D displacement field so that a compressed HD-WFN is obtained (Fig. 1(d)). This method can also generate molded HD-WFN structures with given shapes (Fig. 1(e)), such as double curvature or folded shapes, by carefully designing the 3D compressive displacement fields. Additionally, the proposed method can segment every fiber, locate the fiber bonds, and obtain the principal material axis distribution in the complex fiber morphology using postprocessing (Fig. 1(f)). The generated HD-WFN microstructure models are used for optical property study in this work. All the microstructures in this work are in units of voxels, and they can be transferred to metric units by multiplying a scale factor.

2.3.2. Sparse WFN structure generation

The initial sparse, low-density structure includes a group of randomly distributed straight fibers. The generation of the sparse structure starts by generating a set of separated fibers. The orientation and size of each fiber are given following a given statistical distribution. Each fiber is located in a 3D cubic volume of the same size, where the fiber is assigned a value of 1, while the remaining regions (i.e., air) in the volume are 0. The fiber is simulated with an elliptical cross-section to mimic the compressed fiber (details in Supplementary Material S1. Single fiber generation). The fibers can then be stacked together along the thickness direction to obtain the sparse WFNs V_{Sparse} (Fig. 1(a)).

Different types of WFN can be obtained by controlling the distribution of the fiber orientation θ. For instance, a uniform distribution of θ in $[0, \pi)$ can get an isotropic (isotropic for the in-plane fiber orientation) WFN. A Gaussian distribution of θ leads to an aligned WFN with a principal orientation. A more realistic WFN can be created by using fibers of different widths. Examples include the WFNs made from birch and balsa fibers, where vessels and fibers have significant size variation.

2.3.3. 3D compressive displacement field construction

The compression of the sparse structure following a designed 3D compressive displacement field is a critical procedure in the proposed method. The 3D compressive displacement field is obtained using a purely geometrical method by following the basic assumptions:

- Air is compressible, while the fibers (including the lumen) are incompressible along the thickness direction (z direction in Fig. 1 (a));
- The compressed paper has a uniform thickness distribution.
- The compressive strain for air is the same along the thickness direction (z-direction) at any point (x, y) (Fig. 1(a)).

Based on these assumptions, the 3D compressive displacement fields $w(x, y, z)$ for the sparse WFN can be obtained by first retrieving the 3D compressive strain field $\varepsilon(x, y, z)$ along z direction. This is the key step in

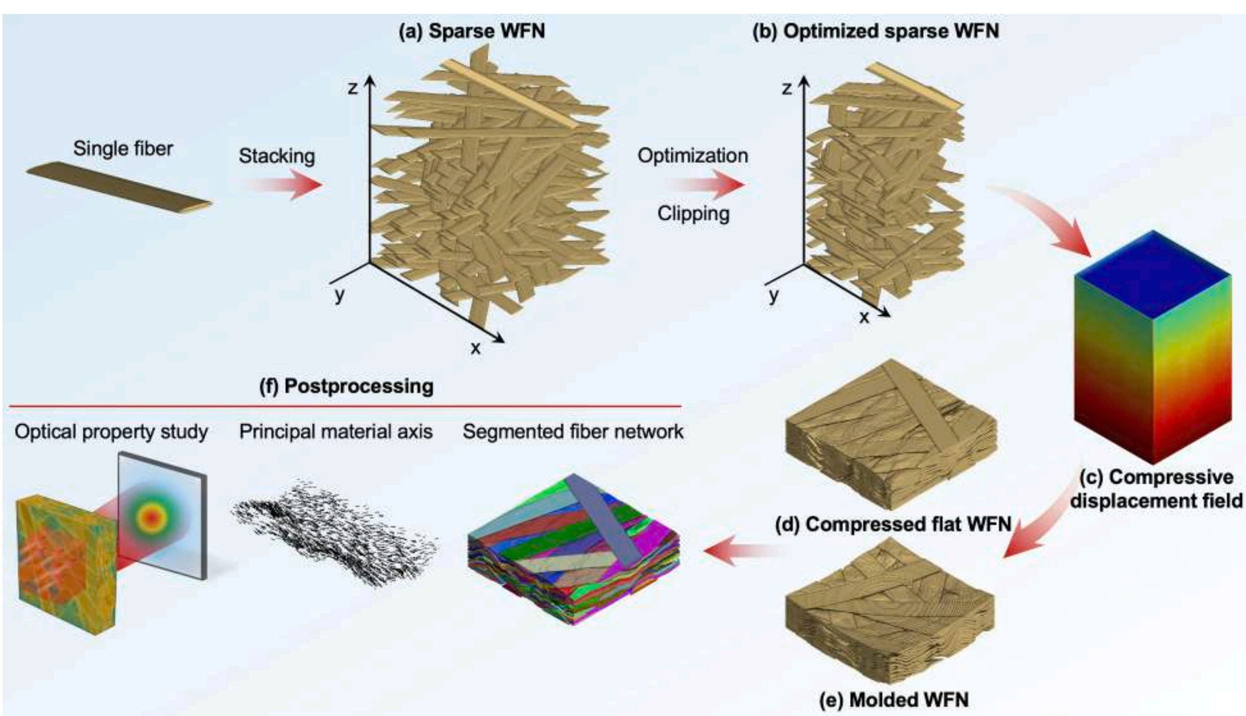

Fig. 1. Flowchart of HD-WFN microstructures generation: (a) sparse WFN by stacking multiple compressed fibers along thickness direction; (b) sparse WFN by optimizing the every fiber location in plane, which is important for reaching a low porosity; (c) 3D displacement field used to deform the sparse WFN; (d, e) the compressed WFN with a flat and double curvature shape; (f) processing to segment every single fiber, detect the local principal material axis and simulate optical scattering.

this method.

The voxel value in the initial sparse WFN microstructure volume is notated as $V_{Sparse}(x,y,z)$, where (x,y,z) is the voxel coordinate (unit of pixel). $V_{Sparse}(x,y,z)$ has a value of 1 and 0 for the voxel (x,y,z) occupied by fiber and by air, respectively. Suppose that the sparse WFN microstructure V_{Sparse} has a thickness of T_{Sparse} (unit of voxel). The total amount of fiber material in the sparse WFN volume V_{Sparse} at location (x, y) along the thickness (z direction) direction is calculated as $M(x,y)$:

$$M(x,y) = \sum_{z=1}^{T_{Sparse}} V_{Sparse}(x,y,z) \tag{1}$$

The thickness of the compressed WFN cannot be thinner than $T_{Compressed}$ (Eq. (2)) since the fibers are assumed incompressible along the z direction (thickness direction).

$$T_{Compressed} = \max_{x,y}(M(x,y)) \tag{2}$$

It means that the thickness of the compressed WFN $T_{Compressed}$ (unit of voxel) is governed by the local region of highest fiber content along z direction in the sparse WFN V_{Sparse}. The compressive strain at every point (x,y,z) in the sparse volume V_{Sparse} can be readily determined since we know 1) the thickness of V_{Sparse} before compression (T_{Sparse}) and after compression ($T_{Compressed}$); 2) the total material amount $M(x,y)$ along z direction (i.e., thickness direction). The compressive strain comes only from the compression of the air. For the voxels (x,y,z) occupied by air, the strain is calculated as

$$\varepsilon(x,y,z)|_{air} = -\frac{T_{Sparse} - T_{Compressed}}{T_{Sparse} - M(x,y)} \tag{3}$$

$T_{Sparse} - T_{Compressed}$ denotes the thickness change of the WFN before and after compression, which is also the thickness change of the air, since the fibers are assumed incompressible. $T_{Sparse} - M(x,y)$ denote the amount of air along z direction in the sparse WFN at the location (x,y). Therefore, $\varepsilon(x,y,z)|_{air}$ measures the relative thickness change (i.e., strain) of the air content at the voxel (x,y,z). For the voxels occupied by fibers (including lumen), we have the compressive strain $\varepsilon(x,y,z)|_{fiber} = 0$ due to the incompressibility assumption.

The 3D compressive displacement map $w(x,y,z)$ along z direction (i.e., thickness direction) can be integrated from the strain field $\varepsilon(x,y,z)$. On the bottom layer ($z = 0$), the displacement is $w(x,y,0) = 0$. Suppose that the displacement at the lower layer $z = z_0$ ($0 \le z_0 \le T_{Sparse} - 1$) in the sparse volume is determined as $w(x,y,z_0)$, the displacement at the neighboring layer $z = z_0 + 1$ can be determined as

$$w(x,y,z_0+1) = w(x,y,z_0) + \varepsilon(x,y,z_0+1), (0 \le z_0 \le T_{Sparse} - 1) \tag{4}$$

For instance, $w(x,y,1)$ can be calculated from $w(x,y,0)$, where $w(x,y,0) = 0$. The 3D displacement fields $w(x,y,z)$ in the whole sparse WFN can be obtained slice by slice from the bottom slice ($z = 0$) to the top slice ($z = T_{Sparse}$) sequentially.

Note that there is no stress analysis involved; the approach is purely geometrical. The directly constructed 3D displacement field considers only the fiber rigidity along the z direction (fiber cross-section). The fiber may easily bend with large shear strain and noise. This is not realistic. This displacement field may lead to a very wavy fiber shape, which reflects low rigidity in x-y plane. The wavy fiber shape is mainly due to the rapid change of the compressive displacement field between neighboring voxels. A smoother compressive displacement field will lead to less wavy fibers, which reflects higher stiffness for the fibers in x-y plane. Therefore, the fiber bending stiffness is also taken into account (rigidity along fiber direction) by smoothing the 3D displacement fields with a moving average smoothing routine (with a convolution kernel size of $11 \times 11 \times 1$) in the x-y plane (see a smoothed displacement map in Fig. 1(c)). This smoothing method is purely geometrical and effective. An example (Fig. S1) demonstrates that the 3D HD-WFNs generated from the displacement without smoothing are significantly noisier compared with those with displacement field smoothing.

2.3.4. Fiber network compression

The value of every voxel in the compressed WFN (Fig. 1(d)) can be obtained from the displacement field $w(x,y,z)$ (Fig. 1(c)) and the sparse WFN V_{Sparse}:

$$V_{Compressed}(x,y,z+w(x,y,z)) = V_{Sparse}(x,y,z) \tag{5}$$

For any point (x,y,z) in the sparse WFN V_{Sparse}, it moves to $(x,y,z+w(x,y,z))$ in the compressed WFN $V_{Compressed}$. It means that the voxel value $V_{Compressed}(x,y,z+w(x,y,z))$ should be the same as $V_{Sparse}(x,y,z)$. The value of 1 and 0 in the compressed WFN volume $V_{Compressed}$ represents fiber and air, respectively. To avoid the boundary effect from the displacement map, only the center part in the compressed WFN $V_{Compressed}$ is kept by removing 9 voxels along each edge in the x and y directions.

2.4. Microstructure refinement

The WFN microstructures can be further refined for more challenging tasks. This work introduces three refined microstructures:

1) WFNs with varied fiber morphologies: The wood fibers in real WFN composites are not perfectly straight and solid. Introducing size variation and curvature into the fibers might be more realistic. Slightly hollow fibers might also be of interest for lower V_f.

2) HD-WFNs with very low porosity: The porosity of the directly compressed WFNs can hardly reach very low, i.e., ~20%. An optimization step that refines the locations for all fibers in the sparse WFN is introduced to improve V_f in the compressed WFNs. The method can lead to the WFN with very high density or low porosity (~20%).

3) Molded WFNs with designated 3D shape: Molding is a very popular process to create 3D products, such as egg cartons, food trays, and various packing products from wood fibers. The HD-WFNs models with given 3D shapes can help simulate the mechanical properties of such products.

2.4.1. WFNs with curved fibers

The fibers are initially straight. We apply an extra in-plane displacement map to each fiber to obtain curved fibers, more similar to experiments. The same method has been used to generate high-fidelity 3D wood microstructure models [29]. These displacement maps, instead of compressing the fibers along the z direction, distort the fibers in the x-y plane to offer more in-plane variation of each fiber. More complicated fiber morphologies can be obtained by carefully designing the in-plane displacement map.

2.4.2. WFN with very low porosity using fiber location optimization

The generation of high-density (or low-porosity) WFNs is challenging. The compressibility of the sparse WFN is limited when many fibers, for statistical reasons, are accumulated in the same local region in the thickness direction (z-axis). The local fiber clustering is also what we have observed in experimental studies [6]. We assume that the cell wall cannot be compressed, which seems reasonable. The WFN cannot be further compressed due to local accumulation of fibers on top of each other in certain regions, even if there are still large porous areas in other locations. Note that the "compression plate" is rigid, so that as soon as one region consists only of incompressible fibers (no air), further compression of the neighboring regions is no longer possible, and no further compression takes place.

The density of the compressed WFN can be improved (i.e., reduce porosity) by optimizing the location of each fiber in the x-y plane while keeping their orientations (Fig. 1(b)). The idea is to reduce the possible local clustering of the fibers in the WFN.

Here, the particle swarm algorithm is used to optimize the locations (in x-y plane) of all fibers simultaneously to reduce the expected porosity, which is calculated as $1 - \mathrm{mean}(M(x,y))/T_{\mathrm{Compressed}}$. The expected porosity can be estimated before WFN compression, since $T_{\mathrm{Compressed}}$ and $M(x,y)$ can be calculated from the sparse WFNs, which is very important for efficiency. In the optimization, each fiber has two degrees of freedom. The fiber locations should not be completely free to move in the x-y plane in the optimization. Instead, in this work, the fibers are only allowed to shift less than 100 voxels in the x and y directions. If we suppose that there are N fibers in the sparse WFN, the optimization has $2N$ degrees of freedom. The fiber locations leading to minimum expected porosity will be used to generate the HD-WFNs after obtaining the corresponding 3D compressive displacement fields.

The fiber optimization procedure is validated on an isotropic sparse structure with 100 fibers. The $M(x,y)$ without and with fiber optimization is shown in Fig. 2(a) and (b), respectively. The optimized $M(x,y)$ (Fig. 2(b)) is far more homogeneous compared with the original one (Fig. 2(a)). The expected porosity decreases from 40.6 % to 21.8 % after fiber location optimization.

2.4.3. Molded 3D HD-WFNs with a designated shape

The molded WFN can be simulated with given molded shapes, such as the flat shape (upper of Fig. 3), the double curvature shape (lower part of Fig. 3), and the folded shape, by carefully designing the 3D displacement fields (see Fig. 3). The HD-WFNs can then be obtained by compressing the initial sparse WFN using the given 3D displacement fields. The 3D displacement map to obtain the flat paper is shown in the upper part of Fig. 3.

To obtain a 3D molded shape, the 3D displacement field is a combination of planar compression and an extra shape molding (lower part of Fig. 3). It can guide the flat paper to any desired shape, such as double curvature and folded shapes. Take a mold with double curvature as an example. A curvature mold is applied afterwards to reshape the paper morphology. The displacement field for the spherical (double curvature) mold shape is written as:

$$w(x,y,z) = R - R \times \cos\left(\mathrm{asin}\left(\frac{\sqrt{(x-x_{\mathrm{m}})^2 + (y-y_{\mathrm{m}})^2}}{R}\right)\right) \quad (6)$$

where R is the radius of the mold. The center of the sphere mold is (x_{m}, y_{m}, R). The compressive displacement field is constant along the z direction at location (x, y). The summation of the two 3D displacement fields (lower part of Fig. 3) can deform the sparse WFN structure to a compressed double curvature HD-WFN. In a similar way, molded WFN with a folded shape can be generated.

2.5. Numerical simulation of optical scattering using ray tracing

The refractive index (RI) difference between the fiber and the "matrix" (air or polymer) in the composites is an important reason resulting in optical scattering in the wood fiber composites. Based on the generated HD-WFN microstructures, the effect of fiber orientation and the addition of a polymer matrix on the optical scattering of HD-WFNs can be studied. In this work, haze is used as the indicator for optical scattering [30]. An incident light beam meets a specimen and exits at the opposite surface of the specimen. Due to the RI difference between wood fiber and air or polymer matrix, the exiting rays will be scattered. Haze [30] is defined as the exit rays with scattered angles larger than 2.5° divided by the total number of transmitted rays. This is a widely used standardized indicator for optical scattering assessment of optical materials.

For efficiency, the ray tracing method based on geometrical optics is used. The ray tracing method can trace ray paths in 3D microstructures without the need for a complex and time-consuming mesh, which is a significant advantage in simplicity and efficiency. It has been used to study the optical scattering of transparent wood composites [27]. The implementation procedure of the ray tracing in a wood-based composite has been described in detail in Ref. [27]. To facilitate the use of this method, the open-source code of ray tracing is shared on GitHub,[2] accompanied by a usage tutorial. The code can be used to study the optical scattering of a composite once given the 3D microstructure model and the RIs of the reinforcements and the matrix of the composite.

In the simulation, on one surface of the 3D microstructure model (Fig. 4), 1000 rays are perpendicularly incident into the sample in a region with a size of 250 × 250 voxels. The rays will deflect their direction at the interface of two optical media due to the RI mismatch between the matrix (polymer or air) and the fibers. The ray tracing method [27] tracks the 3D deflected paths of every ray inside the 3D microstructures until it exits from the back side of the specimen. Many exit rays will be scattered with large ray angles to the incident light. The haze can be determined by analyzing the scattered ray angle distribution of the emergent rays. For simplicity, only the rays that leave the sample from the opposite surface are counted for the haze calculation. This simplification may lead to an error for strongly scattering microstructures due to rays exiting through lateral surfaces. The haze might therefore be underestimated. A larger-scale microstructure can help to reduce the fraction of the rays escaping from the lateral surfaces. However, the generation of large microstructures can be very time-consuming.

In this work, the optical scattering of four materials is studied and compared (Fig. 4), including HD-WFNs: 1) with oriented fibers (Fig. 4(a)); 2) with randomly distributed fibers (Fig. 4(b)); 3) with oriented fibers and impregnated with polymer matrix (Fig. 4(a)); 4) with randomly distributed fibers and impregnated with polymer matrix (Fig. 4(b)). 1) and 2) are transparent paper structures containing fibers and air, and 3) and 4) are wood fiber-polymer composites. The RIs of wood fiber, polymer matrix, and air are given as 1.54, 1.535, and 1, respectively. The composites are all generated from 100 fibers with very similar thickness.

3. Results

A set of high-density (or low-porosity) 3D WFN models with isotropic and oriented fibers is generated. Molded WFNs with given shapes, including double curvature and folded shapes, are simulated. WFNs with curved fibers and fibers of various sizes are also generated. Lastly, we segmented the fibers and assigned spatially varied principal material axes to each fiber, which is important for physical property simulation. The optical properties are studied and compared for different HD-WFN materials.

3.1. WFNs with isotropic fiber orientation

Fig. 5(a) and (b) show the compressed WFNs without and with fiber location optimization. The WFN microstructures include 100 fibers with isotropic orientation and have a size of 482 × 482 voxels in the x-y plane. The fibers are assumed to be fully compressed (i.e., without air in the lumen) and with a width of 80 voxels as well as a thickness of 9 voxels. The elliptical cross-sections present a high aspect ratio to mimic the compressed fibers. The fibers have a relatively smooth shape due to the average smoothing operation of the 3D compressive displacement map, to mimic the effect of fiber stiffness. The porosity P is 44.8% for the compressed WFNs (Fig. 5(a)) without fiber location optimization. The fiber location optimization strategy can reduce the porosity to 27.7% (Fig. 5(b), see the smaller dark void in the cross-section image in the middle panel), which matches well with the real material microstructures observed by SEM (Fig. 5(c)). In Fig. 5(a), the right side of the cross-section image (middle panel) represents a local material accumulation, which limits further compression of the WFNs, even though there are

[2] https://github.com/BinChenOPEN/Composite_Optical_Scattering.

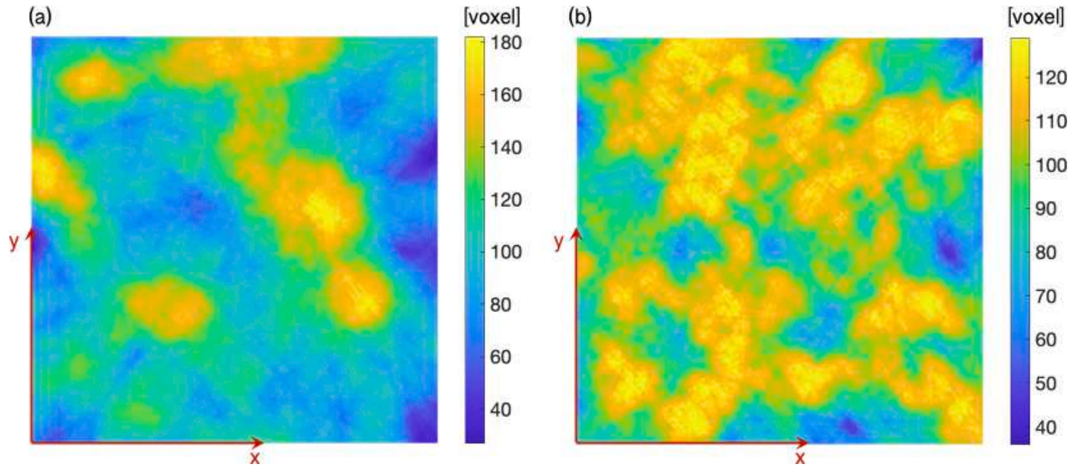

Fig. 2. Total material content distribution $M(x, y)$ of the sparse WFN prior to compression: (a) without and (b) with fiber location optimization procedure. The color denotes the total material amount along the thickness direction (z direction).

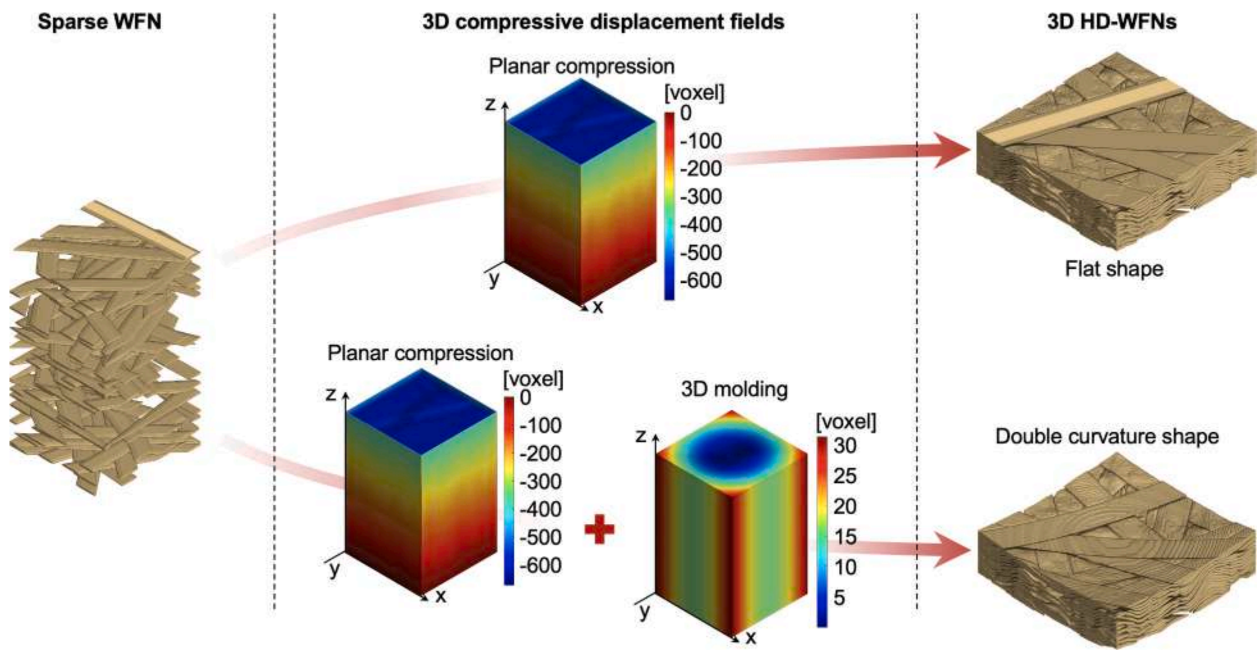

Fig. 3. Generation of compressed 3D HD-WFN microstructure model with given shapes: upper) flat paper and lower) double curvature shape by compressing a sparse WFN following well-designed 3D displacement fields.

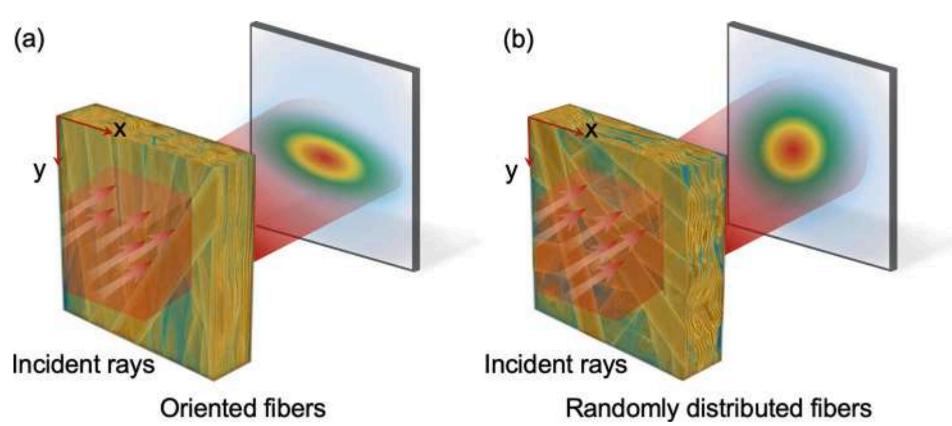

Fig. 4. Ray tracing for optical scattering study in HD-WFNs with (a) oriented fibers with a standard deviation of fiber orientation of $\pi/16$ and (b) isotropic fiber orientation. The HD-WFNs contain either air ("paper") or a polymer matrix (polymer composites).

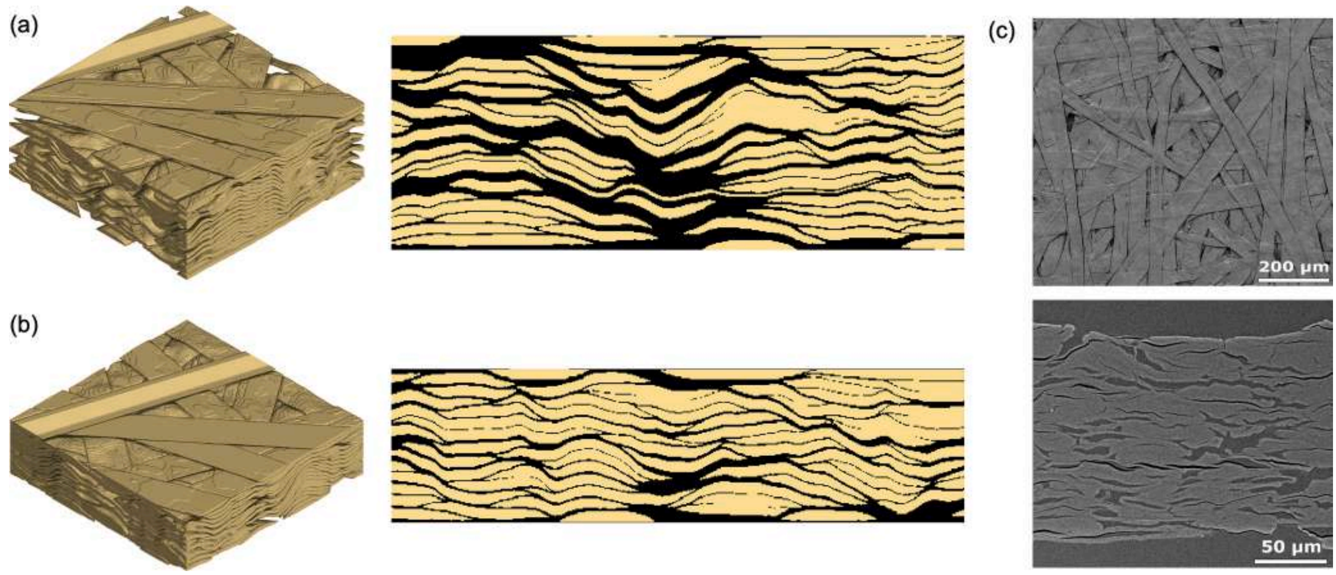

Fig. 5. Compressed WFNs with 100 isotropic fibers: (a) without and (b) with fiber location optimization. (c) SEM images of real random WFN material with a thickness of ~ 170–180 μm and porosity of 24 % in the upper) in-plane and lower) cross-section plane.

large voids on the left. The inhomogeneous fiber distribution contributes to the high porosity of the compressed WFNs, where no fiber location optimization has been used.

3.2. Oriented WFNs

The oriented WFNs (Fig. 6) can be obtained by assigning a Gaussian distribution (mean of 0, standard deviation of $\pi/8$) instead of a uniform distribution for the fiber orientation θ. The mean value of the fiber orientation denotes the material principal orientation. The standard deviation governs the extent of fiber misalignment. Fig. 6(a) and (b) show the obtained oriented WFNs without and with fiber location optimization. The fiber location optimization operation can reduce the porosity from 46.5% (Fig. 6(a)) to 25.1% (Fig. 6(b)). The cross-section images clearly show fewer voids in the WFNs with fiber location optimization (Fig. 6(b)). The fiber alignment along the y-axis in the cross-section images (Fig. 6(a)) can be clearly observed. The generated oriented HD-WFN microstructure (Fig. 6(b)) matches well with the real material microstructures observed by SEM (Fig. 6(c)).

3.3. Molded WFN with designated shapes

The mold forming of paper materials (WFNs) with double curvature (Fig. 7(a)) and folded shape (Fig. 7(b)) is also simulated. The double curvature (spherical) mold (Fig. 7 (a)) has a radius of 2000 voxels, while the fold angle (Fig. 7(b)) has an angle of 157.4°. The generated microstructures can be used to study the mechanical properties of molded WFN products.

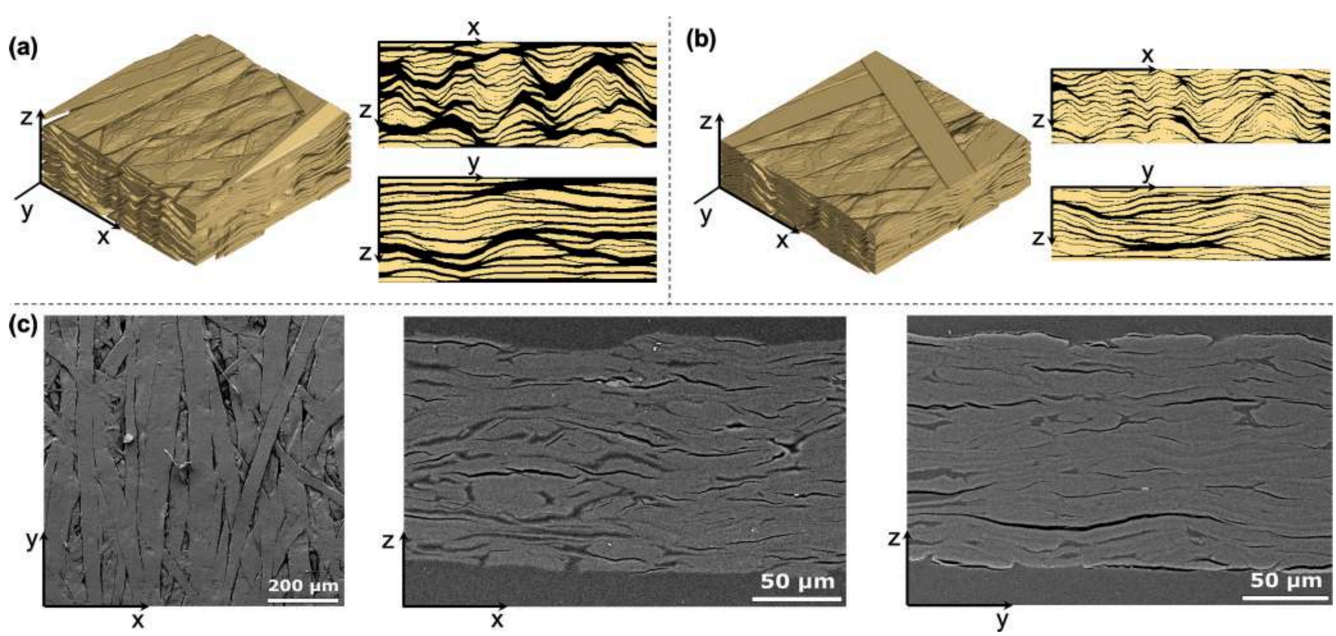

Fig. 6. Compressed WFNs with 100 oriented fibers: (a) without and (b) with fiber location optimization. The fiber orientation follows a Gaussian distribution with a mean value of 0 and a standard deviation $\pi/8$. The 3D structures are on the left, while the cross-section images are shown on the right. (c) SEM images of real oriented WFN material with a thickness of ~ 170–180 μm and porosity of 20 % are shown in the left) x-y, middle) x-z and right) y-z plane.

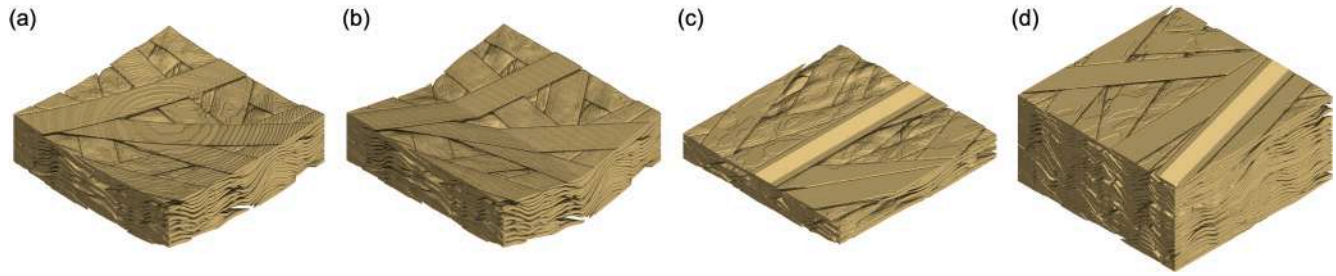

Fig. 7. Molded HD-WFNs from 100 fibers with (a) double curvature and (b) folded shapes; Compressed-oriented HD-WFNs from (c) 50 and (d) 200 fibers with flat shape.

3.4. HD-WFNs with different thickness

HD-WFN materials with three different thicknesses are simulated for both oriented and isotropic WFNs (Table 1). The thickness has a significant impact on the porosity in that thicker structures show lower porosity. A simple thought experiment tells us that with fewer fibers, the probability is high that we will have many regions with large porosity. Remember that as soon as there is a single location with only fully compressed fibers through the thickness (no air), no further compression takes place.

The fiber orientation (oriented or isotropic) has a small effect on porosity (Table 1). The oriented HD-WFNs can generally reach a slightly lower porosity compared with the random ones, which matches well with the prepared real materials (24% for random WFNs against 20% for oriented WFNs). The oriented HD-WFNs with 50, 100, and 200 fibers are shown in Fig. 7(c), Fig. 6(b), and Fig. 7(d), respectively.

The fiber location optimization procedure can significantly increase WFN density (or reduce porosity, Table 1). The reason is that the fiber locations are optimized to reduce the local fiber clustering, which is a key factor in limiting the compressibility of a WFN. The fibers are more evenly distributed after the fiber location optimization procedure. The WFNs can reach very low porosity, i.e., 21.5%, when 200 fibers are included in the microstructure. Such porosity is very close to hot-pressed HD-WFNs (~20%) reported in the literature [31]. The thicker HD-WFN has a lower porosity. HD-WFNs with even lower porosity should be achievable by including an even larger number of fibers (thicker material). When the number of fibers is large enough, the fibers, in theory, show a closer to a uniform distribution in space. In this case, the fiber location optimization operation is less needed. After fiber location optimization, the HD-WFNs with preferred fiber orientation show slightly lower porosity (for the ones with fiber numbers of 100 and 200) compared with those with isotropic fiber orientation.

3.5. HD-WFNs with varied fiber morphologies

More HD-WFNs (Fig. 8) were generated by using other types of fibers: curved fibers (Fig. 8(a)), fibers of various sizes (Fig. 8(b)), and hollow fibers (Fig. 8(c)). In Fig. 8(a), some fibers have obvious curvature (see the fiber along the red straight dashed line). Fig. 8 (b) shows the HD-WFN comprising fibers with different dimensions, which is more realistic compared with a constant fiber size for real wood materials. The fiber width varies from 60 to 120 voxels in this model. The HD-WFNs discussed previously are all composed of completely solid fibers. Under a lower state of compression or due to the springback, fibers may have a central hollow space (lumen) (Fig. 8(c)). The hollow lumen is apparent from the zoomed-in cross-section image in the lower-right panel of Fig. 8(c).

Table 1
Porosity for the compressed HD-WFNs with different numbers of fibers. The oriented WFN has a mean value of 0 and a standard deviation of $\pi/8$ for the fiber orientation.

Fiber angle distribution	Fiber number	Porosity without fiber location optimization (%)	Porosity with fiber location optimization (%)
Oriented fibers	50	52.9	31.4
	100	46.5	25.1
	200	39.8	21.5
Isotropic distribution	50	52.5	31.3
	100	44.8	27.7
	200	39.7	23.9

3.6. Postprocessing of the generated HD-WFN models

3.6.1. Fiber segmentation

To help study the physical properties of WFNs, every fiber in the HD-WFN is segmented (Fig. 9). Such information is very important for the simulation of mechanical properties in the fiber network scale [32]. For every voxel in the initial sparse structure, its counterpart location in the compressed WFN is also known based on the 3D displacement field. Therefore, for every voxel in the compressed WFN, we can inversely determine its location in the initial sparse structure and the corresponding fiber. The fibers can be labeled with different colors in the compressed-oriented WFN (Fig. 9 (a)). A single fiber (Fig. 9 (b)) and a fiber–fiber bond (Fig. 9 (c)) are isolated from the compressed WFN. The fibers show wavy shapes due to the compression and interactions between fibers, which matches well with the observation from SEM images (Fig. 9 (d)) of the real WFN materials.

3.6.2. Interfiber bonds

Interfiber bonds are of critical importance for the mechanical properties of WFNs. In the elastic range, they influence the interfiber stress transfer and stiffness parameters. During failure, they are also very important, although more difficult to analyze. The fiber bond distribution in the compressed HD-WFNs can be determined (Supplementary Material S2. Fiber bond distance). Interfiber bonds (the red regions) are located between fibers (Fig. 10(a) and (b)). Fig. 10(c) presents only the interfiber bond distribution, with the color representing the distance between the fibers. The interfiber distance can reflect the difference in fiber bond strength among the HD-WFNs. Fiber gaps with a distance smaller than a threshold value (1 voxel in this work) are defined as interfiber bonds. The threshold may be determined more accurately in the future based on experimental characterization. The extracted interfiber bond properties are of great interest for numerical modeling of mechanical properties [33,34].

3.6.3. Local fiber orientation distribution

Wood fibers can be described as orthotropic fibers. If a fiber is perfectly straight, the analysis is simplified. The fibers are, however, significantly distorted (Fig. 11 (a)) in the compressed WFNs as well as in real WFNs. The principal material axis varies spatially following the complex morphology of the fiber. Numerical simulation needs to assign orthotropic material properties to the fibers in the local material coordinate system (different at every point). We can obtain the spatial

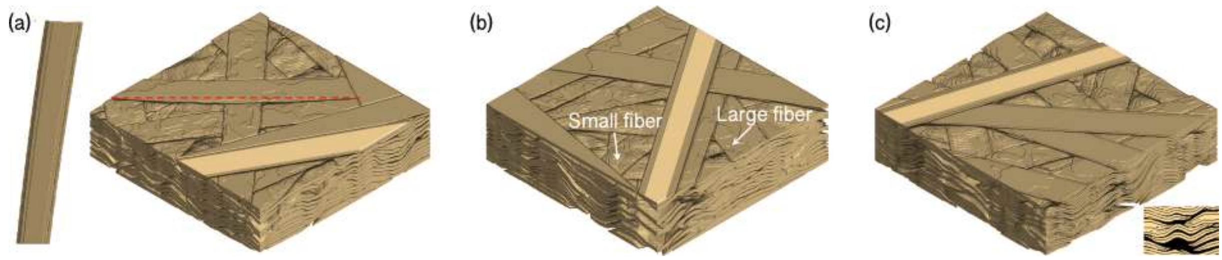

Fig. 8. Compressed HD-WFNs with different morphologies for the fibers: (a) curved fibers, (b) fibers with different dimensions, and (c) hollow fibers.

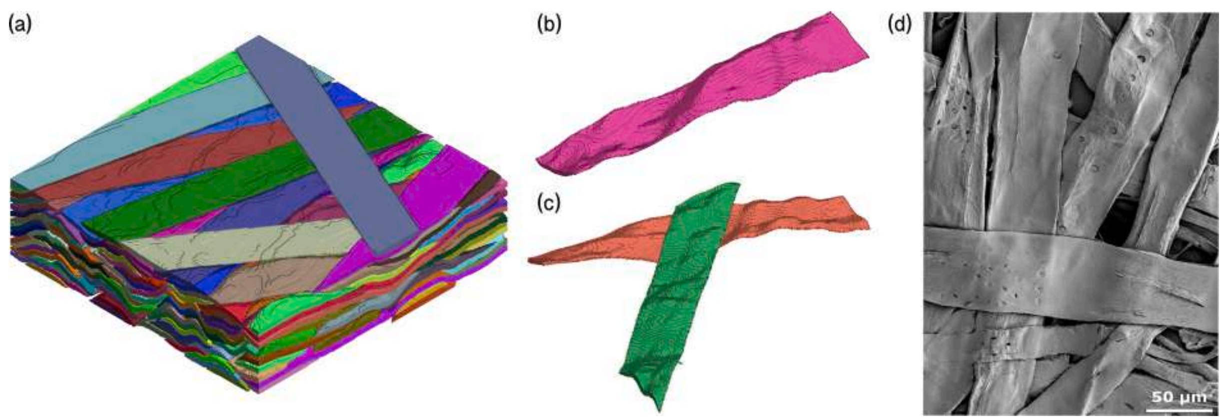

Fig. 9. Compressed WFNs with (a) all fibers being segmented, (b) a segmented single fiber, and (c) a segmented fiber bond; (d) SEM images showing the wavy shape of the fibers in the real WFNs.

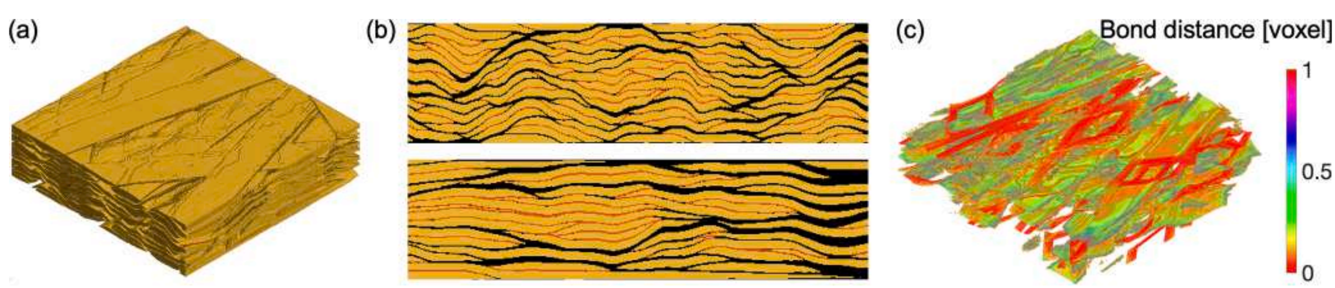

Fig. 10. Fiber bond determination in compressed WFN: WFN with interfiber bonds marked in red color (a) 3D view and (b) cross-sectional view; WFN with (c) varied interfiber bond distance reflecting the fiber bond strength difference. (For interpretation of the references to colour in this figure legend, the reader is referred to the web version of this article.)

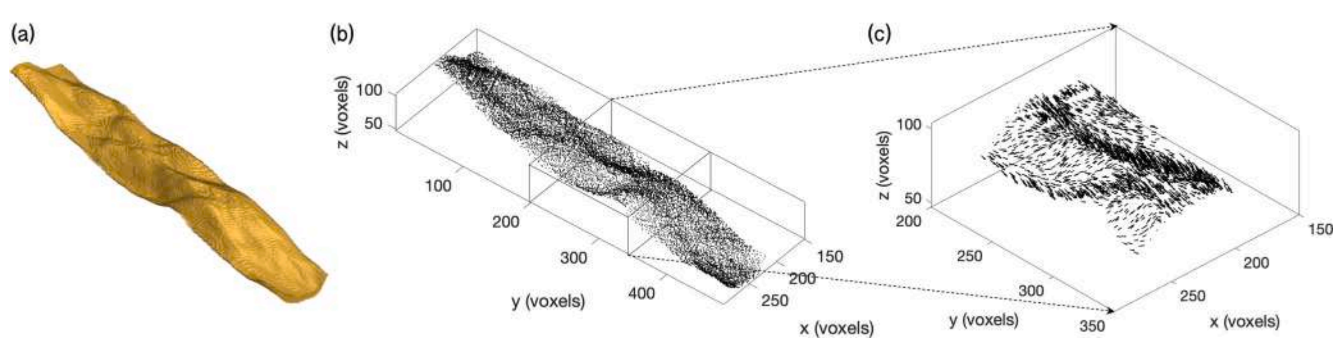

Fig. 11. Compressed paper with different fibers: (a) curved fibers, (b) fibers with different sizes, and (c) hollow fibers.

distribution of the principal material axis for the compressed WFN (Supplementary Material S3. Material principal axis determination). The principal material axis on a distorted fiber (Fig. 11 (a)) is shown in Fig. 11 (b). A zoomed-in region in Fig. 11 (c) shows that the fiber (cell wall) orientation (see the arrow orientation) follows the morphology of the fiber. The local fiber orientation for all points in the compressed HD-WFNs can be determined. It is then possible to accurately assign orthotropic material properties to local regions in all fibers of compressed HD-WFNs.

3.7. Optical scattering of HD-WFNs using simulation

The haze (percentage of scattered light > 2.5°) [30], an indicator for optical scattering of the material, is studied by simulation. The haze concept is slightly modified in this work to indicate the projection of the scattered light (percentage of scattered light > 2.5°) in X and Y directions (Fig. 4). The haze results of HD-WFN materials ("composites") for light transmitted through-the-thickness are obtained and shown in Table 2. For the "paper" materials, the "matrix" is air (fibers and air in the HD-WFN). This is related to materials such as transparent paper used to make engineering drawings. The other material is polymer composites, where the matrix is a polymer with a RI better matched to the RI of the fibers. The projected haze in X and Y directions for a through-thickness light beam (Fig. 4) is presented for those HD-WFN composites, see Table 2. All the WFN microstructures involve 100 fibers. The isotropic HD-WFNs show isotropic optical scattering, while the oriented ones present slightly anisotropic optical scattering. The main result is that the "paper" materials with fibers and air show very high haze in the range 76.6–87.4% whereas polymer matrix composites only show haze in the region 25.9–29.4%, meaning less scattering.

Table 2
Haze of different WFN materials (composites) with air or polymer as "continuous" matrix phase.

HD-WFN composites	Refractive index		Haze (%)	
	Matrix	Wood fiber	X direction	Y direction
Oriented fibers (angle standard deviation: $\pi/16$)	1 (air)	1.54	87.4	76.6
	1.535 (polymer)	1.54	29.4	25.9
Isotropic fibers	1 (air)	1.54	86.0	83.9
	1.535 (polymer)	1.54	27.3	27.4

4. Conclusions

We proposed a simple and efficient method to generate 3D high-density wood fiber network (HD-WFN) microstructure models for numerical simulations. This method first generates a sparse 3D microstructure by stacking several single fibers together without any overlapping. The key procedure uses a purely geometrical method to design a 3D compressive displacement field. The displacement field is generated by assuming compressibility for air and incompressibility for the fibers. A compressed HD-WFN can be obtained by compressing the sparse microstructure following the designed displacement field. As a purely geometrical method, the proposed method can readily control fiber dimensions, orientation, location, number, and material thickness. The major findings in this work include:

- The proposed method can numerically generate 3D HD-WFN models of very high density or low porosity (21.5%), which show strong similarities with real materials.
- The fiber location optimization procedure is the key step to reach such low porosity, since it can reduce the local fiber clustering. The porosity can be further reduced by removing the incompressibility assumption of the fibers. Thicker WFNs might reach lower porosity due to better fiber distribution homogeneity, simply due to statistical distribution reasons.
- The proposed method can readily generate the WFNs with any given molding shape with only negligible extra computational effort.
- The method provides insight into processing-structure relationships. For instance, the fiber location optimization can guide the design of WFN with lower porosity. By shaking the fibers in the plane, the material porosity can be reduced.
- The fiber orientation, i.e., isotropic or oriented fibers, is not so important for material porosity.
- This method can segment every fiber and determine the spatially varied principal material axis at every voxel. This information is important for 1) accurate numerical simulation of physical properties (such as optical and mechanical properties) of HD-WFNs and 2) statistical analysis of the microstructure morphology.
- The extent of interfiber bonds can be determined or controlled in the compressed HD-WFNs. The fiber gap distance difference can reflect the interfiber bond strength variation, which can contribute to more accurate mechanical property simulations.

The generated 3D HD-WFN microstructures are used to study the optical properties of HD-WFN composites. The isotropic HD-WFNs show isotropic optical scattering (large-angle scattering), while the oriented WFNs present slightly anisotropic optical scattering. The impregnation of the HD-WFNs by a RI-matched polymer matrix can significantly reduce the optical scattering. The long-term goal is to train a deep learning model from a large dataset of microstructures for structure–property relationship investigations. Thousands of WFN microstructures can be generated by varying the fiber sizes, shape, orientation, etc. It must be noted that the method is geometrical with no strict physics theory (e.g., stress analysis) for WFN generation. More experimental data can improve the model. The proposed model does not naturally get a periodic RVE, which is critical for the numerical homogenization. Future work will be on generating a periodic RVE.

CRediT authorship contribution statement

Bin Chen: Writing – review & editing, Writing – original draft, Visualization, Validation, Software, Project administration, Methodology, Investigation, Formal analysis, Data curation, Conceptualization. **Erfan Oliaei:** Writing – review & editing, Writing – original draft, Visualization, Data curation. **Lars A. Berglund:** Writing – review & editing, Writing – original draft, Supervision, Project administration, Funding acquisition, Conceptualization.

Declaration of competing interest

The authors declare that they have no known competing financial interests or personal relationships that could have appeared to influence the work reported in this paper.

Acknowledgment

The authors gratefully acknowledge the support from the Knut and Alice Wallenberg Foundation (KAW 2021.0311). The authors also thank the HORIZON AI-TRANSPWOOD (AI-Driven Multiscale Methodology to Develop Transparent Wood as Sustainable Functional Material) project, Grant no. 101138191, co-funded by the European Union. Views and opinions expressed are however those of the author(s) only and do not necessarily reflect those of the European Union or HaDEA. Neither the European Union nor the granting authority can be held responsible for them.

Appendix A. Supplementary data

Supplementary data to this article can be found online at https://doi.org/10.1016/j.matdes.2026.115937.

Data availability

The source code is released on GitHub

References

[1] U. Schenker, J. Chardot, K. Missoum, A. Vishtal, J. Bras, Short communication on the role of cellulosic fiber-based packaging in reduction of climate change impacts,

Carbohydr. Polym. 254 (2021) 117248, https://doi.org/10.1016/j.carbpol.2020.117248.
[2] A.K. Singh, P. Itkor, M. Lee, J. Shin, Y.S. Lee, Promoting sustainable packaging applications in the circular economy by exploring and advancing molded pulp materials for food products: a review, Crit. Rev. Food Sci. Nutr. 63 (2022) 11010–11025, https://doi.org/10.1080/10408398.2022.2088686.
[3] N. Simon, K. Raubenheimer, N. Urho, S. Unger, D. Azoulay, T. Farrelly, J. Sousa, H. van Asselt, G. Carlini, C. Sekomo, M.L. Schulte, P.O. Busch, N. Wienrich, L. Weiand, A binding global agreement to address the life cy cle of plastics, Science 373 (2021) (1979) 43–47, https://doi.org/10.1126/science.abi9010.
[4] M. Didone, P. Saxena, E. Brilhuis-Meijer, G. Tosello, G. Bissacco, T.C. Mcaloone, D. C.A. Pigosso, T.J. Howard, Moulded Pulp Manufacturing: Overview and prospects for the Process Technology, Packag. Technol. Sci. 30 (2017) 231–249, https://doi.org/10.1002/pts.2289.
[5] Y. Liu, S. Ma, F. Wang, L. Wang, Advances in Research of Molded Pulp for Food packaging, J. Renew. Mater. 11 (2023) 3831–3846, https://doi.org/10.32604/jrm.2023.028251.
[6] E. Oliaei, F. Berthold, L.A. Berglund, T. Lindström, Eco-Friendly High-Strength Composites based on Hot-pressed Lignocellulose Microfibrils or Fibers, ACS Sustain. Chem. Eng. 9 (2021) 1899–1910, https://doi.org/10.1021/acssuschemeng.0c08498.
[7] A. Khakalo, A. Vishtal, E. Retulainen, I. Filpponen, O.J. Rojas, Mechanically-induced dimensional extensibility of fibers towards tough fiber networks, Cellul. 24 (2017) 191–205, https://doi.org/10.1007/s10570-016-1102-z.
[8] T. Joelsson, G. Pettersson, S. Norgren, A. Svedberg, H. Höglund, P. Engstrand, High strength paper from high yield pulps by means of hot-pressing, Nord. Pulp Paper Res. J. 35 (2020) 195–204, https://doi.org/10.1515/npprj-2019-0087.
[9] S. Saeb, P. Steinmann, A. Javili, Aspects of Computational Homogenization at Finite Deformations: a Unifying Review from Reuss' to Voigt's Bound, Appl. Mech. Rev. 68 (2016) 50801, https://doi.org/10.1115/1.4034024.
[10] R. Talreja, 10-Modelling defect severity for failure analysis of composites, in: W. Van Paepegem (Ed.), Multi-Scale Continuum Mechanics Modelling of Fibre-Reinforced Polymer Composites, Woodhead Publishing, 2021: pp. 275–306. https://doi.org/https://doi.org/10.1016/B978-0-12-818984-9.00010-X.
[11] W. Tian, X. Chao, M.W. Fu, L. Qi, An advanced method for efficiently generating composite RVEs with specified particle orientation, Compos. Sci. Technol. 205 (2021) 108647, https://doi.org/10.1016/j.compscitech.2021.108647.
[12] J.W. Simon, A Review of recent Trends and challenges in Computational Modeling of Paper and Paperboard at Different Scales, Arch. Comput. Meth. Eng. 28 (2021) 2409–2428, https://doi.org/10.1007/s11831-020-09460-y.
[13] S. Bargmann, B. Klusemann, J. Markmann, J.E. Schnabel, K. Schneider, C. Soyarslan, J. Wilmers, Generation of 3D representative volume elements for heterogeneous materials: a review, Prog. Mater Sci. 96 (2018) 322–384, https://doi.org/10.1016/j.pmatsci.2018.02.003.
[14] A. Karakoç, A. Miettinen, J. Virkajärvi, R. Joffe, Effective elastic properties of biocomposites using 3D computational homogenization and X-ray microcomputed tomography, Compos. Struct. 273 (2021) 1–10, https://doi.org/10.1016/j.compstruct.2021.114302.
[15] E.L.G. Wernersson, S. Borodulina, A. Kulachenko, G. Borgefors, Characterisations of fibre networks in paper using micro computed tomography images, Nord. Pulp Paper Res. J. 29 (2014) 468–475, https://doi.org/10.3183/npprj-2014-29-03-p468-475.
[16] J.X. Liu, Z.T. Chen, K.C. Li, A 2-D lattice model for simulating the failure of paper, Theor. Appl. Fract. Mech. 54 (2010) 1–10, https://doi.org/10.1016/j.tafmec.2010.06.009.
[17] Y.H. Ma, H.X. Zhu, B. Su, G.K. Hu, R. Perks, The elasto-plastic behaviour of three-dimensional stochastic fibre networks with cross-linkers, J. Mech. Phys. Solids 110 (2018) 155–172, https://doi.org/10.1016/j.jmps.2017.09.014.
[18] K.J. Niskanen, M.J. Alava, Planar random networks with flexible fibers, Phys. Rev. Lett. 73 (1994) 3475–3478, https://doi.org/10.1103/PhysRevLett.73.3475.
[19] A. Kulachenko, T. Uesaka, Direct simulations of fiber network deformation and failure, Mech. Mater. 51 (2012) 1–14, https://doi.org/10.1016/j.mechmat.2012.03.010.
[20] T. Verho, S. Fortino, P. Hradil, T. Turpeinen, K. Immonen, A. Harlin, D. Sandquist, Biocomposite modeling by tomographic feature extraction and synthetic microstructure reconstruction, Compos. Sci. Technol. 230 (2022) 109713, https://doi.org/10.1016/j.compscitech.2022.109713.
[21] J. Sliseris, H. Andrä, M. Kabel, B. Dix, B. Plinke, O. Wirjadi, G. Frolovs, Numerical prediction of the stiffness and strength of medium density fiberboards, Mech. Mater. 79 (2014) 73–84, https://doi.org/10.1016/j.mechmat.2014.08.005.
[22] GeoDict - The Digital Material Laboratory, (n.d.). https://www.math2market.com/ (accessed February 12, 2026).
[23] G. Gaiselmann, C. Tötzke, I. Manke, W. Lehnert, V. Schmidt, 3D microstructure modeling of compressed fiber-based materials, J. Power Sources 257 (2014) 52–64, https://doi.org/10.1016/j.jpowsour.2014.01.095.
[24] Z. Pan, Y. Liang, M. Tang, Z. Sun, J. Hu, J. Wang, Simulation of performance of fibrous filter media composed of cellulose and synthetic fibers, Cellul. 26 (2019) 7051–7065, https://doi.org/10.1007/s10570-019-02605-8.
[25] B. Lin, Y. Bai, B.X. Xu, Data-driven microstructure sensitivity study of fibrous paper materials, Mater. Des. 197 (2021) 109193, https://doi.org/10.1016/j.matdes.2020.109193.
[26] X. Yang, L.A. Berglund, Recycling without Fiber Degradation - strong Paper Structures for 3D Forming based on Nanostructurally Tailored Wood Holocellulose Fibers, ACS Sustain. Chem. Eng. 8 (2020) 1146–1154, https://doi.org/10.1021/acssuschemeng.9b06176.
[27] B. Chen, S. Popov, L.A. Berglund, Ray scattering in fiber-reinforced transparent wood composites – wood microstructural effects and virtual camera simulation, Opt. Mater. (amst). 162 (2025) 116953, https://doi.org/10.1016/j.optmat.2025.116953.
[28] E. Oliaei, C. Montanari, L. Li, H. Chen, P. Olsén, L. Berglund, Translucent Biocomposites from Hot-pressed Wood Fibers and Poly(limonene acrylate), ACS Appl. Mater. Interfaces 17 (2025) 43522–43535, https://doi.org/10.1021/acsami.5c07130.
[29] B. Chen, C. Montanari, S. Popov, L.A. Berglund, A distortion-map-based method for morphology generation in multi-phase materials - application to wood, Compos. Sci. Technol. 244 (2023) 110262, https://doi.org/10.1016/j.compscitech.2023.110262.
[30] A. International, Test Method for Haze and Luminous Transmittance of Transparent Plastics, 08 (2000) 3–4. https://doi.org/10.1520/D1003-00.
[31] X. Yang, F. Berthold, L.A. Berglund, High-Density Molded Cellulose Fibers and Transparent Biocomposites based on Oriented Holocellulose, ACS Appl. Mater. Interfaces 11 (2019) 10310–10319, https://doi.org/10.1021/acsami.8b22134.
[32] S. Borodulina, H.R. Motamedian, A. Kulachenko, Effect of fiber and bond strength variations on the tensile stiffness and strength of fiber networks, Int. J. Solids Struct. 154 (2018) 19–32, https://doi.org/10.1016/j.ijsolstr.2016.12.013.
[33] U. Hirn, R. Schennach, Fiber-Fiber Bond Formation and Failure: Mechanisms and Analytical Techniques, in: W. Batchelor, D. Söderberg (Eds.), Trans. of the XVIth Fund. Res. Symp. Oxford, 2017, Fundamental Research Committee (FRC), Manchester, 2017: pp. 839–863. https://doi.org/10.15376/frc.2017.2.839.
[34] M. Jajcinovic, W.J. Fischer, U. Hirn, W. Bauer, Strength of individual hardwood fibres and fibre to fibre joints, Cellul. 23 (2016) 2049–2060, https://doi.org/10.1007/s10570-016-0895-0.